

# Link Design for Non-Directed Wireless Infrared Communications

John R. Barry

Joseph M. Kahn

School of ECE

Department of EECS

Georgia Institute of Technology

University of California

Atlanta, Georgia, 30332-0250

Berkeley, California, 94720

barry@ee.gatech.edu

jmk@eecs.berkeley.edu

Tel: (404) 894-1705

Tel: (510) 643-8848

Fax: (404) 853-9959

Fax: (510) 642-2739

## ABSTRACT

We optimize the design of a short-range communication system using non-directed line-of-sight infrared radiation. We propose a receiver structure comprising a spherical thin-film optical filter and a truncated spherical lens, which can significantly outperform an optimized planar-filter system. The passband of the spherical filter can be made arbitrarily narrow, without constraining the field of view, by using an arbitrarily large filter radius. We argue that a truncation angle of  $90^\circ$  will maximize the receiver field of view when a spherical filter is used. We jointly optimize the transmitter radiation pattern and receiver optical components. Numerical results show that 269 mW of transmitted signal power is sufficient to achieve 100 Mb/s throughout a 4-m radius cell with high background irradiance.

*Key Words:* wireless communications, thin-film filters, non-imaging concentrators.

---

Supported by an IBM Faculty Development Award, by NSF under grant number NCR-9308968, and by the Siemens Corporation.

Published in *Applied Optics*, 1995, vol. 34, no. 19, July 1995, pp. 3764-3776.

## I. INTRODUCTION

The push for higher data rates in wireless computing, wireless video, and wireless multimedia applications has motivated recent interest in wireless infrared communication [1]—[8]. As a medium for short-range wireless communication, infrared radiation enjoys three primary advantages over radio. First, the infrared spectrum represents an immense, unregulated bandwidth. Second, infrared radiation does not pass through walls or other opaque barriers, allowing the operation of high-speed links in every room of a building without interference. Third, there is no multipath fading with infrared systems using intensity-modulation and direct detection, because the relative area of the square-law detector is large, typically greater than 10,000 square wavelengths, and this provides an inherent spatial diversity.

Infrared has some drawbacks as well. Although multipath propagation obviates the need for a strict line-of-sight (LOS) path between the transmitter and receiver, an infrared link is still susceptible to severe shadowing; an infrared receiver cannot be carried in a shirt pocket, for example. Also, infrared links have a limited range, because the noise from ambient light is high, and also because the square-law nature of a direct-detection receiver doubles the effective path loss (in dB) when compared to a linear detector.

Non-directed infrared links, which do not require alignment between transmitter and receiver, can be categorized as either LOS or diffuse; a LOS link requires an unobstructed LOS path for reliable communication, whereas a diffuse link relies instead upon reflections from the ceiling or other reflectors. LOS links require less power than diffuse links, but diffuse links are more robust to shadowing. Except for a brief discussion in Sect. III-E, this paper considers only LOS non-directed links.

The dominant impairment in a non-directed link is background light, which is typically a combination of fluorescent light, sunlight, and incandescent light. These light sources emit power over a broad range of wavelengths, with a significant fraction of this power falling within the wavelength band of sensitivity of silicon photodiodes.

There are two ways to mitigate the effects of background light; the first is to use a narrow-linewidth optical source, such as a single- or nearly single-frequency laser diode, in combination with a narrow-band optical filter to reject out-of-band ambient light. The second is to introduce an optical lens between the transmitter and receiver to provide optical gain. Together, the lens and filter make up the optical front end. Ideally, we would like the front end to

act as an ideal optical band-pass filter, providing a large optical gain  $G$  across a narrow passband of width  $\Delta\lambda$ , and rejecting all other wavelengths. Furthermore, we would like the front end characteristics to be invariant to angle of incidence. When these ideal conditions are met, the shot-noise-limited electrical signal-to-noise ratio (SNR) after photodetection is proportional to  $G/\Delta\lambda$ , the gain-to-bandwidth ratio. The problem of achieving a high SNR can thus be reformulated as a problem of devising an optical front end with a large gain-to-bandwidth ratio over a wide field of view (FOV).

This paper proposes two optical front ends comprising a thin-film optical filter and a truncated spherical lens. In the first, a planar thin-film filter is placed between the lens and the photodetector, and in the second, a spherical thin-film filter is placed upon the surface of the lens. We will see that, in the limit of large lens radius, the spherical-filter system approaches the ideal front end described in the previous paragraph. Unfortunately, practical constraints on receiver size and weight may result in a small lens radius, in which case the optical gain is a strong function of angle of incidence, so that the optimization procedure involves more than just maximizing a gain-to-bandwidth ratio.

Sect. II summarizes the properties of thin-film optical filters. In Sect. III we examine the optical gain performance of the truncated spherical lens with optical filter, and explain why the spherical filter outperforms the planar filter. In Sect. IV we present a procedure for the joint optimization of the transmitter radiation pattern and receiver optical front end. We close by presenting typical optimization results which support the viability of high-speed communication using non-directed infrared radiation.

## II. THIN-FILM OPTICAL FILTERS

An efficient narrow-band optical filter can be made using multiple layers of thin dielectric films. Unfortunately, the phase shift through the layers changes with angle of incidence, causing dramatic changes in the filter characteristics at non-normal incidence. This angle dependence is critical in wide-FOV applications. The purpose of this section, therefore, is to summarize the effect of angle of incidence on the performance of thin-film optical filters, and to present a simple Butterworth model for later use.

## II-A. Theoretical Transmission

A thin-film optical filter consists of a stack of  $K - 2$  thin dielectric layers with varying thicknesses and varying indices of refraction. Let  $n_1$  and  $n_K$  denote the refractive index of the input and output medium, respectively, and let  $n_2$  through  $n_{K-1}$  (and  $d_2$  through  $d_{K-1}$ ) denote the refractive indices (and thicknesses) of the intervening layers. For the case when equal power is contained in the transverse-electric (TE) and transverse-magnetic (TM) polarization states, the total fraction of power transmitted through the filter, assuming lossless dielectrics, is given by:

$$T(\theta_1) = 1 - \frac{1}{2} ( |\rho_{TE}|^2 + |\rho_{TM}|^2 ), \quad (1)$$

where the reflection coefficients  $\rho_{TE}$  and  $\rho_{TM}$  are defined by the following set of recursive equations [10]—[12]:

$$\rho = \frac{N_1 - \eta_2}{N_1 + \eta_2}, \quad (2)$$

$$N_k = \begin{cases} n_k / \cos \theta_k & \text{for TE} \\ n_k \cos \theta_k & \text{for TM} \end{cases}, k \in \{2, \dots, K\}, \quad (3)$$

$$\eta_k = N_k \frac{\eta_{k+1} \cos \beta_k + j N_k \sin \beta_k}{N_k \cos \beta_k + j \eta_{k+1} \sin \beta_k}, k \in \{2, \dots, K\}, \quad (4)$$

$$\theta_k = \sin^{-1} \left( \frac{n_{k-1}}{n_k} \sin \theta_{k-1} \right), k \in \{2, \dots, K\}. \quad (5)$$

Here,  $\theta_k$  is the angle made by the light ray as it passes from medium  $k$  to medium  $k + 1$ ,  $\eta_k$  is the effective complex-valued index “seen” by the lightwave as it enters medium  $k$ , and  $\beta_k = 2p \cos(\theta_k) n_k d_k / \lambda$ , where  $\lambda$  is the wavelength of the light in a vacuum [10]. Starting with  $\eta_K = N_K$ , (4) can be applied recursively to arrive at  $\eta_2$ , which when substituted into (2) yields  $\rho_{TE}$  or  $\rho_{TM}$ , depending on the initialization of the  $\{N_k\}$  as either TE or TM in (3).

A single-layer anti-reflection (AR) coating is a special case of a multi-layer dielectric stack, and hence its transmission can be calculated using (1)—(5) with  $K = 3$ ,  $n_2$  equal to the refractive index of the coating, and  $d_2$  equal to the thickness of the coating. Similarly, when  $K = 2$ , (1)—(5) specify the angle-dependent transmission at a single dielectric interface between two media with indices of refraction  $n_1$  and  $n_2$ .

For purposes of illustration, consider the typical 25-layer, three-cavity thin-film optical filter described by  $(\text{LH})^2\text{L}^2(\text{HL})^4(\text{LH})^4\text{L}^2(\text{HL})^2$  [12]. Each layer is one quarter-wave optical thickness (QWOT) with respect to  $\lambda_{normal} = 850$  nm. (1 QWOT =  $\lambda_{normal}/4n$ , where  $n$  is the refractive index of the film.) In Fig. 1 we show the transmission of this filter as a function of wavelength for a number of different angles of incidence, as calculated using (1)—(5), assuming the low index is  $n_L = 2$ , the high index is  $n_H = 3.5$ , the input index is  $n_1 = 1$ , and the output index  $n_K = 1.8$ . The curves are labeled with the angle of incidence  $\theta$  (or  $\theta_1$  in (5)). At normal incidence, the filter is well-approximated by a third-order Butterworth filter with center wavelength  $\lambda_{normal} = 850$  nm and bandwidth  $\Delta\lambda = 36.3$  nm. As the angle of incidence increases to  $30^\circ$ , the spectral shape and bandwidth remain unchanged, while the center wavelength shifts to shorter wavelengths. For angles of incidence near  $60^\circ$  and higher, however, the spectral shape is seen to change considerably.

Define  $\hat{\lambda}(\theta)$  as the center wavelength of the transmission passband for angle of incidence  $\theta$ . It satisfies  $\hat{\lambda}(0) = \lambda_{normal}$ . In Fig. 2 we plot the fractional shift  $\hat{\lambda}(\theta)/\lambda_{normal}$  versus  $\theta$  for the filter of Fig. 1. The dashed curve in the figure is described by the analytic approximation [13]:

$$\hat{\lambda}(\theta) = \lambda_{normal} \sqrt{1 - (n_1/n_s)^2 \sin^2 \theta} , \quad (6)$$

where  $n_1$  is the index of the input layer and  $n_s$  is an effective index for the spacer layer; it is found empirically by fitting the approximate curve to the actual one in Fig. 2 [11][13], yielding  $n_s = 2.293$ . The figure shows that this approximation is quite accurate.

Let  $\lambda_0$  denote the wavelength of the transmitted signal, and let  $\hat{\theta}$  denote the angle at which the center wavelength coincides with  $\lambda_0$ , so that  $\hat{\lambda}(\hat{\theta}) = \lambda_0$ . We refer to  $\hat{\theta}$  as the filter orientation. With this definition, (6) becomes:

$$\hat{\lambda}(\theta; \hat{\theta}) = \lambda_0 \sqrt{\frac{n_s^2 - n_1^2 \sin^2 \theta}{n_s^2 - n_1^2 \sin^2 \hat{\theta}}} . \quad (7)$$

Comparing (7) to (6), we see that the parameters  $\hat{\theta}$  and  $\lambda_{normal}$  are interchangeable, in the sense that both completely characterize the wavelength shift, assuming  $n_1$  and  $n_s$  are known. In practice, however,  $\hat{\theta}$  is the more useful quantity, because its optimal value, as derived in Sect. IV, is nearly independent of  $n_s$  and  $\Delta\lambda$ , whereas the corresponding optimal value for  $\lambda_{normal}$  is a strong function of both  $n_s$  and  $\Delta\lambda$ .

The tendency for the center wavelength to shift to shorter wavelengths at non-normal incidences makes it difficult to obtain an optical filter that has both a narrow passband and a wide FOV. As we explore in Sect. IV, there is an optimal bandwidth that trades off the opposing goals of minimizing the admitted noise and maximizing the FOV.

## II-B. Butterworth Model

We next introduce a simplified model for thin-film filters which extracts only those features that are important to system design. We assume that the spectral shape of the filter has an  $m$ -th order Butterworth characteristic, and that this spectral shape remains the same for all angles of incidence. (The validity of this assumption will be addressed shortly.) We assume that the center wavelength shift is given by (7). Finally, we assume that the peak transmission is  $T_0$ . ( $T_0$  is typically 0.4 to 0.9, because of imperfect dielectrics [12], and also because of inherent losses in metal-dielectric blocking filters that are often used to reject the transmission peaks at wavelengths longer than the primary peak near  $\lambda_{normal}$  [11][13][14].)

With these assumptions, the performance of a thin-film optical filter is characterized by only two primary parameters, the bandwidth  $\Delta\lambda$  and orientation  $\hat{\theta}$ : for a single light ray with wavelength  $\lambda_0$  incident at an angle  $\theta$ , the filter transmission is:

$$T(\theta; \Delta\lambda, \hat{\theta}) = \frac{T_0}{1 + \left( \frac{\lambda_0 - \hat{\lambda}(\theta; \hat{\theta})}{\Delta\lambda/2} \right)^{2m}} . \quad (8)$$

The design of the optical filter thus boils down to specifying the two parameters  $\Delta\lambda$  and  $\hat{\theta}$ ; see Sect. IV. The remaining three parameters ( $n_s$ ,  $m$ , and  $T_0$ ) are generally fixed by technology, and should be chosen as large as possible.

The dashed curves in Fig. 1 show how the simplified model of (8) (with  $\lambda_0$  replaced by  $\lambda$ ) compares to the actual filter transmission. We see that the spectral shape of the passband begins to change for angles of incidence above  $30^\circ$ . At  $\theta = 75^\circ$ , the shape has broadened considerably and exhibits severe passband ripple. The cause of this variation is the ‘‘polarization effect;’’ the rates of change of center wavelength as a function of  $\theta$  are different for the TE and TM polarization modes [12][14].

Fortunately, polarization effects are not critical in our application, because we are not concerned with the filter shape at all wavelengths. Rather, we are only concerned with the filter transmission at the operating wavelength  $\lambda_0$ . For example, suppose the operating wavelength is  $\lambda_0 = 810$  nm. In Fig. 3 we compare the actual angle-dependent transmission of the filter in Fig. 1, as computed using (1)—(5) assuming  $\lambda_0 = 810$  nm, to that predicted by the Butterworth model of (8). The agreement between the two is good, and so in the remainder of the paper we will use the Butterworth model to characterize thin-film filters. This will greatly simplify the filter optimization procedure of Sect. IV, because it will allow us to alter the filter bandwidth and orientation without redesigning a new filter from scratch.

By definition,  $T(\hat{\theta}) = T_0$ . The field of view of a planar thin-film filter can be measured by the angular bandwidth  $\theta_c$ , defined by  $T(\hat{\theta} + \theta_c) = T_0/2$ . (Note that the filter transmission is not symmetric about  $\hat{\theta}$  when  $\hat{\theta}$  is nonzero, and so  $\theta_c$  does not completely characterize the field of view in this case.) An estimate of  $\theta_c$  can be found from (8), with the following approximation being accurate when  $\hat{\theta} \approx 0$ :

$$\theta_c \approx \sin^{-1} \left( \frac{n_s}{n_1} \sqrt{\frac{\Delta\lambda}{\lambda_0}} \right). \quad (9)$$

This implies that the bandwidth of a planar filter (with  $\hat{\theta} \approx 0$ ) must be extremely large to achieve a full field of view ( $\theta_c = 90^\circ$ ); specifically, the bandwidth must satisfy  $\Delta\lambda = \lambda_0 / (n_s/n_1)^2$ , where  $(n_s/n_1)^2$  is typically around 5.

### III. THE TRUNCATED SPHERICAL LENS

To collect sufficient signal power, the receiver in a non-directed link must use a photodetector with a large area. Unfortunately, the high capacitance of large-area photodetectors is a major obstacle to the construction of a wide-band, low-noise preamplifier [4]. It is therefore desirable to use a wide-FOV optical antenna to increase the photodetector effective area. The resulting optical gain is very beneficial; in particular, as discussed in Sect. IV, the electrical SNR ratio is very nearly proportional to optical gain. Although not considered here, one way to achieve optical gain over a wide FOV is to use an array of narrow-FOV non-imaging concentrators, each pointing in a different direction [5]. A less complex alternative is a truncated spherical lens, of which the hemispherical lens is a special case. Its benefit in the context of non-directed communication was first noted by Kotzin and Marhic [2][6]. As we shall see,

optical gains of more than 4 dB are practical. In this section we propose two methods for combining a truncated spherical lens with a thin-film optical filter, and calculate the effective optical gain of each.

### III-A. Gain Calculation for LOS Radiation

Consider a truncated spherical lens with truncation angle  $\theta_p$ , refractive index  $n$ , and radius  $R$  placed concentrically upon a circular photodiode with area  $A = \pi r^2$ , as shown Fig. 4 [2][3][4][6][7][15][17]. We propose two such systems, differing in the placement of the optical filter. In the planar-filter system of Fig. 4-a, a planar filter is placed between the lens and the detector, and in the spherical-filter system of Fig. 4-b, a spherical filter is deposited or bonded directly onto the lens surface. The optical gain for both systems can be calculated using the expanded diagram of Fig. 4-c, as outlined below.

Assume a line-of-sight configuration with a wide collimated beam of uniform irradiance  $p$  (having units of  $W/cm^2$ ) incident at the receiver. As shown in Fig. 4-c, the beam makes an angle  $\psi$  with respect to the photodetector surface normal. Consider a single ray from the beam making an angle  $\theta_0$  with the lens surface normal; it will be attenuated by a factor  $T(\theta_0)$  as it enters the lens, where the angle-dependent transmission factor  $T(\theta_0)$  accounts for reflection loss (planar-filter case) or filter loss (spherical-filter case), as calculated using (1)—(5). The ray is then refracted towards the center of the sphere, making an angle  $\theta_2$  with the normal to the lens truncation plane. Extending this notation, let  $T(\theta_2)$ ,  $T(\theta_3)$ , and  $T(\theta_4)$  represent the transmission at the lens output, planar filter (if any), and detector input, respectively, all calculated using (1)—(5).

When the entire lens system is absent, the power intercepted by the photodetector is  $pA\cos(\psi)$ . With the lens system in place, the detected power increases to  $pA_{eff}(\psi)$ , where the effective area  $A_{eff}(\psi)$  is defined by:

$$A_{eff} = \int_{S_0} T(\theta_0)T(\theta_2)T(\theta_3)T(\theta_4)\cos(\theta_0)dS, \quad (10)$$

where the integration is performed over the portion  $S_0$  of the lens surface for which light passing through will eventually hit the detector.  $S_0$  is easily estimated using a simple ray-tracing technique. The optical gain  $G(\psi)$  provided by the lens is the ratio of the detected powers:  $G(\psi) = A_{eff}(\psi) / A\cos(\psi)$ .

### III-B. Hemispherical Lens

#### III-B.1. Numerical Examples

For the special case of hemispherical lens ( $\theta_t = 90^\circ$ ), normal incidence ( $\psi = 0$ ), and no reflection and filter losses ( $T(\theta_i) = 1$ ), a simple geometric argument shows that the gain  $G(0) \equiv G$  satisfies:

$$r = r\sqrt{G} - \sqrt{R^2 - r^2}G \tan\left(\text{asin}\frac{r\sqrt{G}}{R} - \text{asin}\frac{r\sqrt{G}}{nR}\right). \quad (11)$$

In Fig. 5 we plot this  $G(0)$  versus lens radius  $R$  for indices  $n \in \{1.3, 1.5, 1.8\}$ , assuming  $A = 1 \text{ cm}^2$ . (The curves labeled  $\theta_{max}$  will be discussed later; see Sect. III-C.) We see that the gain is a monotonically increasing function of lens radius. Furthermore, for large radii, the gain approaches an asymptote of  $n^2$ , the thermodynamic limit for passive concentrators [2][15]. Inspection of Fig. 5 reveals the following rule of thumb: most of the asymptotic gain is achieved when the lens radius exceeds the detector radius by a factor of  $n^2$ .

To calculate the gain at non-normal incidence, we resort to a numerical ray-tracing method based on (10). Consider Fig. 6-b (Fig. 6-a and Fig. 6-c will be discussed in Sect. III-C.); it illustrates the effect of angle of incidence on gain for a hemispherical ( $\theta_t = 90^\circ$ ) lens with index  $n = 1.8$ , radius  $R = 2 \text{ cm}$ , and a detector area of  $A = 1 \text{ cm}^2$ . The curve labeled “ideal” shows how  $G(\psi)$  varies with  $\psi$  when there are no reflection losses or filter losses ( $T(\theta_i) = 1$ ). The dotted line is  $n^2$ , the normal-incidence gain assuming infinite lens radius. The gain is seen to vary only slightly with angle, always staying within 0.3 dB of  $n^2$ .

Reflections can significantly reduce the gain, especially at non-normal incidence. To illustrate the dangers of ignoring reflections, consider the same lens, without any AR coatings or index matching, so that the gap between the lens and the detector is filled with air. In this case, the curve labeled “uncoated” in Fig. 6-b results. The precise methods for calculating the angle-dependent transmission factors  $\{T(\theta_i)\}$  due to reflections at the lens input, lens output, and detector input are presented in the second column of Table 1. A sharp drop in gain occurs near  $\sin^{-1}(1/n) = 34^\circ$ , the critical angle of the 1.8-index lens, because light trying to exit the bottom of the lens experiences total internal reflection at larger angles. This results in a narrow FOV that is unacceptable for non-directed applications.

The effects of reflections can be reduced significantly by the careful placement of anti-reflection (AR) coatings and index-matching compounds within the system. For example, when the lens has a single-layer AR coating with index 1.38 and thickness 1.04 QWOT, and the detector has a single-layer coating with index 2.0 and thickness 1.42 QWOT, and the index matching layer has the same index as the lens (see Table 1), the curve labeled “coated” in Fig. 6-b results. Even at the extreme angle of  $\psi = 80^\circ$ , the gain with index-matching and AR coating comes within 1.5 dB of the ideal. A procedure for designing the AR coatings and index-matching layers will be presented in Sect. IV.

Of course, an optical filter is absolutely necessary in most applications, and hence we are most concerned with the optical gain achieved when an optical filter is present. Compare the two curves labeled “planar” and “spherical” in Fig. 6-b, which result from the planar and spherical filter systems of Fig. 4-a and Fig. 4-b, respectively. As summarized in Table 1, the filter bandwidth in both cases is 15 nm, the AR coatings in both cases are identical to those described in the previous paragraph, and the filter orientation  $\hat{\theta}$  is  $45^\circ$  and  $15^\circ$  for the planar and spherical filters, respectively. Observe that the gain of the spherical system is nearly omnidirectional. In contrast, the gain of the planar system is confined to a narrow FOV near  $\hat{\theta} = 45^\circ$ . Thus, although both systems are equally effective at mitigating background light, only the spherical system would be useful in a wide-FOV application. The FOV of the planar system could be expanded by increasing the filter bandwidth, at the cost of increasing the power of admitted background light.

Recent experimental work has demonstrated the wide-FOV capabilities of a spherical optical filter; as part of a prototype 50-Mb/s non-directed infrared link, Marsh and Kahn have implemented a hemispherical filter-lens combination, achieving a 30-nm bandwidth with a  $70^\circ$  FOV [16].

### III-B.2. Angle Distribution for Hemispherical Filter

The superiority of the hemispherical filter over the planar filter, as illustrated in Fig. 6-b, is best explained with the aid of the density functions  $f_\psi^{(0)}(\theta_0)$  and  $f_\psi^{(2)}(\theta_2)$ , which describe the angular distribution of detected light as it enters and exits the lens, respectively ( $\theta_0$  and  $\theta_2$  are illustrated in Fig. 4-c). Specifically, for a collimated beam of uniform irradiance impinging on the lens at an angle  $\psi$  from the detector normal, define  $f_\psi^{(0)}(\theta)\Delta\theta$  as the fraction of the detected power that enters the lens with an angle of incidence  $\theta_0$  in the infinitesimal interval  $[\theta, \theta + \Delta\theta)$ , assuming there are no reflection losses. Similarly, define  $f_\psi^{(2)}(\theta)\Delta\theta$  as the fraction of the detected power that exits the lens with

an angle of incidence  $\theta_2$  in the range  $[\theta, \theta + \Delta\theta)$ . By considering only detected power in these definitions, we are equivalently restricting consideration to light passing through the subset  $S_0$  of the lens surface in (10). Note that, by definition, both  $f_\psi^{(0)}(\theta)$  and  $f_\psi^{(2)}(\theta)$  integrate to unity over the interval  $0 \leq \theta \leq \pi/2$ .

Using numerical methods, we calculated the density functions assuming  $\theta_t = 90^\circ$ ,  $R = 2$  cm,  $n = 1.8$ , and  $A = 1$  cm<sup>2</sup>; the results are presented in Fig. 6. Fig. 6-a shows that light destined to strike the detector enters the hemispherical lens at nearly normal incidence. Specifically, the input angle of incidence is confined to a narrow range of  $(0, \theta_{max})$ , where  $\theta_{max} \approx 31^\circ$  for this example. (An analytic expression for  $\theta_{max}$  will be given in (13).) In contrast, Fig. 6-b shows that light destined to strike the detector can exit the hemispherical lens with any angle of incidence in the range  $(0, 90^\circ)$ .

Without reflection or filter losses, the optical gain of a hemispherical lens is approximately  $n^2$  for all  $\psi$ . After accounting for filter losses (but not reflection losses), the angle-dependent gain decreases by a factor of  $\bar{T}(\psi)$ , the averaged filter transmission. Since the angles of incidence through a spherical and planar filter are described by  $f_\psi^{(0)}(\theta)$  and  $f_\psi^{(2)}(\theta)$ , respectively,  $\bar{T}(\psi)$  is given by:

$$\begin{aligned} \bar{T}(\psi) &= \int_0^{\pi/2} f_\psi^{(0)}(\theta) T(\theta; \Delta\lambda, \hat{\theta}) d\theta && \text{(hemispherical)} \\ \bar{T}(\psi) &= \int_0^{\pi/2} f_\psi^{(2)}(\theta) T(\theta; \Delta\lambda, \hat{\theta}) d\theta && \text{(planar)} \end{aligned} \quad (12)$$

where the filter transmission  $T(\theta; \Delta\lambda, \hat{\theta})$  may be modeled using (8). The dashed curves superimposed onto the density functions of Fig. 6-a and Fig. 6-b illustrate the filter transmission  $T(\theta; \Delta\lambda, \hat{\theta})$ ; the filter bandwidth  $\Delta\lambda$  is 15 nm in both cases, whereas the filter orientation  $\hat{\theta}$  is  $15^\circ$  and  $45^\circ$  for Fig. 6-a and Fig. 6-b, respectively. For a given angle of incidence  $\psi$ , the averaged filter transmission  $\bar{T}(\psi)$  may be calculated by integrating the product of the dashed curve in Fig. 6 with the corresponding density function  $f_\psi^{(i)}(\theta)$ . Fig. 6-a shows that most of the incident light always falls within the passband of the filter, regardless of  $\psi$ , thus explaining the wide FOV of the spherical filter, despite its narrow bandwidth. On the other hand, Fig. 6-b shows that the incident light falls within the passband of the filter only when  $\psi$  is near  $45^\circ$ , thus explaining the narrow FOV of the planar filter.

### III-C. Non-Hemispherical Lens

So far we have focused on the hemispherical examples of Fig. 6-b, for which the truncation angle was fixed at  $\theta_t = 90^\circ$ . Changing this truncation angle has a significant impact on the gain properties of the lens. In Fig. 6-a and Fig. 6-c we repeat the examples of Fig. 6-b, changing only the truncation angle to  $\theta_t = 70^\circ$  and  $\theta_t = 110^\circ$ , respectively. As before, the transmission factors were calculated per Table 1. Consider first the curves labeled “ideal,” which assume no reflection losses. Most striking is the observation that the gain is not omnidirectional, as it was for the hemispherical lens. When  $\theta_t = 70^\circ$ , the gain is maximum at large angles of incidence. On the other hand, when  $\theta_t = 110^\circ$ , the gain is confined to a FOV of less than  $70^\circ$ .

As before, our primary concern is in the net gain of the systems using an optical filter. The curves labeled “planar” and “spherical” in Fig. 6-a through Fig. 6-c show that, although the FOV of the planar-filter systems are not a strong function of  $\theta_t$ , the FOV of the spherical-filter systems are, with a truncation angle of  $90^\circ$  being superior to  $70^\circ$  and  $110^\circ$  for the particular spherical filter considered. The interplay between  $\theta_t$  and FOV will be explored further below, where we argue that, when using a spherical filter, the FOV is maximized by  $\theta_t = 90^\circ$ .

Let  $\theta_{max}$  specify the angle spread at the input of a lens with truncation angle  $\theta_t$ , so that light eventually striking the detector surface enters the lens with angle of incidence confined to the range  $[0, \theta_{max}]$ . Clearly, to maximize the FOV when using a spherical filter, we want  $\theta_{max}$  to be small; although the shape of the density function  $f_\psi^{(0)}(\theta)$  can affect the FOV of a spherical filter to some extent, the discussion of Sect. III-B.2 suggests that  $\theta_{max}$  has the dominant effect on FOV. It is easy to show that:

$$\theta_{max} = \sin^{-1} \left\{ \frac{nr}{R} \sqrt{1 + (R/r)^2 \cos^2 \theta_t} \right\} . \quad (13)$$

Therefore, the FOV of a spherical filter is maximized by choosing the lens radius as large as possible. (This is also desirable from the point of view of maximizing the optical gain.) Furthermore, (13) shows that the FOV of a spherical filter is maximized when the truncation angle is  $90^\circ$ . For this reason, we shall limit consideration to hemispherical lenses in the remainder of the paper.

### III-D. Achieving Arbitrarily Narrow Bandwidth with Full FOV

Observe from (13) that  $\theta_{max} = \sin^{-1}(nr/R)$  when  $\theta_t = 90^\circ$ , in which case  $\theta_{max} \rightarrow 0$  as  $R \rightarrow \infty$ . This is illustrated in Fig. 5, where  $\theta_{max}$  is plotted versus  $R$ , assuming  $A = 1 \text{ cm}^2$ . In principle, therefore, the electrical shot-noise-limited SNR can be made arbitrarily large by first choosing an arbitrarily small filter bandwidth  $\Delta\lambda$ , and then choosing  $R$  large enough to make  $\theta_{max}$  sufficiently small. Here,  $\theta_{max}$  is “sufficiently small” when the angle-dependence of the spherical filter transmission is negligible; the following procedure quantifies this idea.

First, choose  $\Delta\lambda$  as small as required to achieve a desired SNR. The angular bandwidth  $\theta_c$  is then specified by (9). The last step is to choose  $R$  large enough that all detected rays pass through the filter at angles falling within the angular passband. This is roughly equivalent to the condition  $\theta_{max} \leq \theta_c$ ; hence, from (9) and (13), a full FOV requires that  $R$  satisfy:

$$R \geq \frac{nr}{n_s/n_1} \sqrt{\frac{\lambda_0}{\Delta\lambda}}. \quad (14)$$

For example, a lens radius of at least 2.3 cm is required to achieve a full field of view when  $\Delta\lambda = 30 \text{ nm}$ ,  $\lambda_0 = 810 \text{ nm}$ ,  $n = 1.8$ ,  $n_s/n_1 = 2.293$ , and  $\pi r^2 = 1 \text{ cm}^2$ .

Without any restrictions on the lens radius  $R$ , the above procedure solves the problem of designing a narrow-band, wide-FOV optical filter. We are particularly interested in addressing the case of portable receivers, however, where there are strict size and weight limitations. The remainder of the paper assumes that  $R$  is finite, assuming a value of  $R = 2 \text{ cm}$  in all numerical examples.

### III-E. Gain Calculation for Isotropic Radiation

Suppose that, rather than a LOS plane wave, the hemispherical-filter system of Fig. 4-b is subject to isotropic radiation having unity flux ( $\text{W}/\text{m}^2/\text{sr}$ ). Isotropic radiation is a convenient model for background radiation or for a link using a diffuse transmitter. Savicki and Morgan have shown that, ignoring reflections, the flux inside the lens is either  $n^2$  or 0, depending on the angle of view, with the flux being 0 only when the viewing direction is such that incoming light would have to violate Snell’s law [17]. If the lens radius satisfies:

$$R \geq \frac{nr}{\sqrt{1 - n^2 \cos^2 \theta_t}}, \quad (15)$$

then Snell's law is never violated, so that every point on the detector surface is subject to isotropic radiation with flux  $n^2$ . In this case, the total gain (neglecting reflection and filter losses) is  $n^2$ . For example, when  $\theta_t = 90^\circ$ ,  $R$  must be  $nr$  in order for the total gain to be  $n^2$ .

#### IV. JOINT OPTIMIZATION of TRANSMITTER and FILTER

In this section we jointly optimize the transmitter radiation pattern and optical filter, which will yield better results than if we tried to optimized each independently. Let  $H$  (with units  $\text{cm}^{-2}$ ) denote the memoryless transfer function of the channel, so that an optical intensity of  $P$  at the transmitter results in a signal irradiance of  $HP$  at the receiver. The detected photocurrent is then  $r_p HPA_{eff}$ , where  $r_p$  is the photodetector responsivity, and  $A_{eff}$  is the effective area of the photodetector from (10).

Suppose the background irradiance is white and isotropic, so that the background irradiance per unit filter bandwidth  $p_{bg}$  is constant, independent of wavelength, receiver position, and receiver orientation. Let  $A_{bg}$  denote the effective area of the optical front end as seen by the background light; because the signal is not isotropic,  $A_{bg}$  is not equal to  $A_{eff}$ . The detected background light is then  $p_{bg}\Delta\lambda A_{bg}$ , where  $\Delta\lambda$  is the filter bandwidth; this induces a white Gaussian shot-noise current with power spectral density  $qr_p p_{bg}\Delta\lambda A_{bg}$ , where  $q$  is the charge of an electron. Therefore, if  $P$  is the average transmitted optical power, the bit-error rate for on-off keying with bit rate  $B$  is  $Q(\sqrt{SNR})$ , where  $Q(x) = (2\pi)^{-1/2} \int_x^\infty e^{-t^2/2} dt$ , and where:

$$SNR = \frac{r_p H^2 P^2 A_{eff}^2}{q p_{bg} \Delta\lambda A_{bg} B}. \quad (16)$$

The optical front end should be designed so as to maximize the figure of merit  $A_{eff}^2 / A_{bg} \Delta\lambda$ , which is related to the gain-to-bandwidth ratio described in the introduction.

As discussed in Sect. III-E,  $A_{bg}$  simplifies to  $n^2 A$  when the lens radius  $R$  satisfies (15), where  $n$  is the lens index. After accounting for filter losses, the effective area becomes:

$$A_{bg} = n^2 T_0 A, \quad (17)$$

where  $T_0$  is the peak filter transmission. This result is applicable, although somewhat pessimistic, even when the background light source is a distant point source rather than being isotropic; it results from the line-of-sight analysis when the detector is aligned with the noise source ( $\psi = 0^\circ$ ) and the optical gain is set to  $n^2 T_0$ .

As specified in (10),  $A_{eff}$  accounts for lens gain, tilt loss, and filter and reflection losses. To a first-order approximation, the lens gain is  $n^2$ , the tilt loss is  $\cos\psi$ , and the combination of filter and reflection losses is  $T_0$ , so that  $A_{eff} \approx n^2 T_0 A \cos\psi$ . It is convenient to express  $A_{eff}$  in terms of this first-order approximation:

$$A_{eff} = \gamma(\psi) n^2 \bar{T}(\psi) A \cos\psi, \quad (18)$$

where we have introduced two new parameters;  $\gamma(\psi) \approx 1$  measures the efficiency with which the lens achieves a gain of  $n^2$ , neglecting reflection and filter losses, and  $\bar{T}(\psi) \leq T_0$  accounts for all reflection and filter losses:

$$\gamma(\psi) = \frac{1}{n^2 A \cos\psi S_0} \int \cos\theta_0 dS, \quad (19)$$

$$\bar{T}(\psi) = \frac{\int_{S_0} T(\theta_0) T(\theta_2) T(\theta_3) T(\theta_4) \cos\theta_0 dS}{\int_{S_0} \cos\theta_0 dS}. \quad (20)$$

For example, from the curve labeled “ideal” in Fig. 6-b we see that  $0.94 \leq \gamma(\psi) \leq 1.06$  for all  $\psi$  when  $\theta_t = 90^\circ$ ,  $R = 2$  cm,  $n = 1.8$ , and  $A = 1$  cm<sup>2</sup>. Unlike (12), which ignored reflection losses, (20) accounts for all reflection and filter losses.

Substituting (17) and (18) into (16) yields:

$$SNR = \frac{r_p H^2 P^2 \gamma^2 \bar{T}(\psi)^2 \cos^2\psi}{q P_{bg} \Delta\lambda T_0 B} \cdot n^2 A. \quad (21)$$

Observe that, to a first-order approximation, the SNR is linearly proportional to detector area, and proportional to the square of the lens index. Thus,  $n$  and  $A$  should be chosen as large as possible. (Strictly speaking, both  $\gamma$  and  $\bar{T}(\psi)$  are functions of  $A$  and  $n$ , but the dependence is weak and of little consequence in practice.) The transmitter radiation pattern and optical filter should be designed so as to maximize the figure of merit  $(H\gamma\bar{T}(\psi))^2/\Delta\lambda$ , as discussed below.

#### IV-A. Transmitter Optimization

For purposes of illustration we consider a cylindrical cell of radius  $d$ , as illustrated in Fig. 8; the height of the cell is  $h_{max} - h_{min}$ , and the transmitter is centrally located a distance  $h_{min}$  above the top of the cell. For each possible receiver location, let  $\psi$  denote the angle between the orientation of the transmitter (down) and the position vector of the receiver. Define  $\psi_B = \tan^{-1}(d/h_{max})$  and  $\psi_C = \tan^{-1}(d/h_{min})$ . Let  $P$  denote the instantaneous power of the transmitter. The axial symmetry of the cell calls for an axially symmetric transmitter radiation pattern  $R(\psi)$  ( $\text{sr}^{-1}$ ), defined so that  $PR(\psi)$  is the emitted optical intensity per unit solid angle at an angle  $\psi$  from the orientation of the transmitter. Integrating  $PR(\psi)$  over a hemisphere must yield  $P$ , so that:

$$2\pi \int_0^{\pi/2} R(\psi) \sin\psi \, d\psi = 1. \quad (22)$$

A receiver with effective area  $A_{eff}$  pointing straight up and located at an angle  $\psi$  and vertical distance  $h$  from the source will detect a total power of  $PR(\psi)d\Omega$ , where  $d\Omega$  is the solid angle subtended by the detector,  $d\Omega = \cos^2\psi A_{eff}/h^2$ . In this case, the channel transfer function is  $H(\psi) = R(\psi)\cos^2\psi/h^2$ .

Observe that, for any  $\psi$ , the SNR is at its minimum when the path loss is greatest, or in other words, when the receiver is located at the boundary of the cell, either on line  $\overline{AB}$  or  $\overline{BC}$  in Fig. 8. If we optimize  $R(\psi)$  so as to maximize the minimum SNR in the cell, it is easy to show that the optimum radiation pattern  $R_o(\psi)$  forces the SNR to be constant at all points on the cell boundary, independent of  $\psi$ :

**Theorem 1.** The optimal radiation pattern  $R_o(\psi)$ , maximizing the minimum SNR in the cell, is that which makes the SNR equal to the same constant at each point on the lines  $\overline{AB}$  and  $\overline{BC}$ .

See Appendix A for a proof. Since the noise irradiance is assumed to be constant throughout the cell, an optimal radiation pattern will also cause the detected signal power to be constant on the cell boundary. To determine an explicit expression for  $R_o(\psi)$ , we set the detected power on the cell boundary  $H(\psi)PA_{eff}$  equal to a constant  $P_o$ , yielding:

$$R_o(\psi) = \frac{P_o}{P} \cdot \frac{h^2(\psi)}{A_{eff}\cos^2\psi}, \quad (23)$$

where  $h(\psi)$  is the vertical distance between source and transmitter on the cell boundary;  $h(\psi) = h_{max}$  for  $\psi \in [0, \psi_B)$  and  $h(\psi) = d/\tan(\psi)$  for  $\psi \in [\psi_B, \psi_C]$ . Note from (23) how  $R_o(\psi)$  compensates for the angle-dependent losses

associated with the optical filter, so that any modifications of the filter characteristics will modify the optimal radiation pattern. The detected power on the cell boundary results from (22):

$$P_o = \frac{P}{2\pi \int_0^{\psi_c} \frac{h^2(\psi) \sin \psi}{A_{eff} \cos^2 \psi} d\psi} . \quad (24)$$

Substituting into (21), the SNR on the cell boundary with optimum radiation pattern is:

$$SNR = \frac{rP^2}{qp_{bg}T_0B} \cdot n^2A \cdot \Gamma, \quad (25)$$

where we have introduced the figure of merit  $\Gamma$ :

$$\Gamma = \frac{1}{\Delta\lambda} \left( 2\pi \int_0^{\psi_c} \frac{h^2(\psi) \sin \psi}{\gamma(\psi) \bar{T}(\psi) \cos^3 \psi} d\psi \right)^{-2} . \quad (26)$$

With transmitter optimization per (23), the minimum SNR will be maximized when the filter bandwidth, orientation, and AR coatings are designed so as to maximize the figure of merit  $\Gamma$ .

#### IV-B. Joint Optimization of Optical Filter and AR Coatings

Theorem 1 allows us to express the radiation pattern in terms of the parameters of the optical front end; the final step in our optimization procedure is to optimize the optical front end so as to maximize (26). In particular, for the optical front ends of Fig. 4-a and Fig. 4-b, the following parameters should be jointly optimized:  $\Delta\lambda$ ,  $\hat{\theta}$ ,  $n_{c,1}$ ,  $d_{c,1}$ ,  $n_{m,3}$ ,  $n_{m,4}$ ,  $n_{c,2}$ , and  $d_{c,2}$ . (The spherical-filter front end of Fig. 4-b does not require an outer AR coating, so that  $n_{c,1}$  and  $d_{c,1}$  need not be considered.) Our approach is to first specify the refractive indices  $n_{c,1}$ ,  $n_{c,2}$ ,  $n_{m,3}$ , and  $n_{m,4}$  based on practical constraints, and then to choose the remaining parameters so as to maximize the figure of merit (26).

In practice, a continuum of values for  $n_{c,1}$  and  $n_{c,2}$  are not available, but rather the designer must choose them from a discrete set of practical values. The optimal coating index  $n_{c,1}$  will be near  $\sqrt{n}$ , where  $n$  is the refractive index of the lens. For example, the common coating material magnesium fluoride has a refractive index of  $n_{c,1} = 1.38$  [11], and thus makes a good choice for a lens with index  $n = 1.8$ .

The refractive index of the detector coating may be chosen in a similar manner. First, consider the planar configuration of Fig. 4-a. To minimize reflection loss between the lens and the planar filter, the intervening space should be filled with an index-matching compound. By choosing the index of the compound to equal the index  $n$  of the lens, reflections at the lens-compound interface can be eliminated. As always, reflections at the input and output of the planar filter can be subsumed into the transmission characteristic of the filter itself and need not be considered separately. The only remaining issue is to minimize the reflections between the filter output and the photodetector input. Again, an index matching compound should be used between the filter and detector to minimize reflection loss. The best refractive index for this matching layer is not obvious, since it depends on the output wave impedance of the optical filter and the input wave impedance of the AR-coated photodetector. We assume that the refractive index of both index-matching layers ( $n_{m,3}$  and  $n_{m,4}$ ) in Fig. 4-c is  $n$ , the index of the lens. With this assumption, the detector coating  $n_{c,2}$  should be chosen near  $\sqrt{nn_d}$ , where  $n_d$  is the refractive index of the detector; the refractive index of silicon at 810 nm is  $n_d = 3.686$  [18]. We will assume  $n_{c,2} = 2.0$  (SiO) in our numerical examples.

With the refractive indices  $n_{c,1}$ ,  $n_{c,2}$ ,  $n_{m,3}$ , and  $n_{m,4}$  specified, it remains to specify the parameters  $\Delta\lambda$ ,  $\hat{\theta}$ ,  $d_{c,1}$ , and  $d_{c,2}$  so as to maximize (26). This can be accomplished, for example, using a numerical grid search. In Table 2 we present sample optimization results for both planar-filter and hemispherical-filter systems, considering cells with radius  $d \in \{3 \text{ m}, 4 \text{ m}, 5 \text{ m}, 8 \text{ m}\}$ . The vertical dimensions of the cells in all cases are  $h_{min} = 1.5 \text{ m}$  and  $h_{max} = 2.4 \text{ m}$ . The lens and detector are similar to that considered previously, with  $\theta_t = 90^\circ$ ,  $n = 1.8$ ,  $R = 2 \text{ cm}$ , and  $A = 1 \text{ cm}^2$ .

The first two rows of Table 2 specify the optimal bandwidth and orientation of the filter. (The optimal normal-incidence wavelength may be obtained from the optimal orientation using the relationship  $\lambda_{normal} = \lambda_0 / (1 - (n_1/n_s)^2 \sin^2 \hat{\theta})^{1/2}$ ). The fifth row is  $P_o/P$ , the fraction of the transmitted power that is detected on the cell boundary, as calculated from (24). The final row is  $P_{req}$ , the required average optical power of the transmitter to achieve a shot-noise-limited SNR of 13.5 dB, assuming the photodetector responsivity is 0.53 A/W, the background irradiance per unit bandwidth is  $p_{bg} = 5.8 \text{ } \mu\text{W}/(\text{cm}^2 \cdot \text{nm})$ , which corresponds to bright sky light [1], and a bit rate of  $B = 100 \text{ MHz}$ . ( $SNR_{req} = 13.5 \text{ dB}$  was chosen because it is the required average electrical SNR for a baseband on-off-keyed system with additive Gaussian noise to achieve a bit-error rate of  $10^{-6}$ .)

Consider the 4-m radius cell, and compare the planar filter results with the hemispherical filter results. The optimal bandwidth decreases from 70.1 nm for the planar filter to 12.3 nm for the hemispherical filter; the hemispher-

ical filter thus rejects  $70.1/12.3 = 7.6$  dB more noise power than does the optimal planar filter. Furthermore, the price paid for this superior noise rejection in terms of filter loss is not great; the ratio  $P_o/P$  is only 0.19 dB optical (0.38 dB electrical) less than that for the planar filter. The hemispherical filter thus nets a 7.2-dB improvement in SNR when compared to the optimal planar filter, which translates to a 3.6-dB reduction in required optical power.

The improvement in FOV provided by the hemispherical filter over the planar filter is illustrated in Fig. 9, which shows polar plots of the optimal transmitter radiation pattern, as specified by (23), and the corresponding effective area  $A_{eff}(\psi)$ . Fig. 9-a and Fig. 9-b apply to the planar-filter system, and Fig. 9-c and Fig. 9-d apply to the hemispherical-filter system. Observe how the optimized transmitter compensates for the severe loss of the planar-filter system near normal incidence. The optical gain for the hemispherical-filter system is nearly omnidirectional, on the other hand, so that the transmitter radiation pattern is nearly  $\cos^{-3}(\psi)$  for  $\psi \in [0, \psi_B)$ , which compensates for path loss.

Precautions must be taken to ensure eye safety with the higher optical powers of Table 2. A laser diode can be made eye safe by destroying its spatial coherence and spreading the radiation over an extended emitting aperture. New eye-safety regulations are likely to restrict diffuse power densities at wavelengths near 850 nm to levels of about  $370 \text{ W/m}^2$  for continuous viewing [7][19].

The power requirements of the last row of Table 2 are summarized in Fig. 10, where we plot the transmitter power requirement versus cell radius. In addition to a 100 Mb/s system, we also show results for a 10 Mb/s system. When the cell radius is 3 m, the 10-Mb/s system requires only 41 mW of optical power to achieve an SNR of 13.5 dB. Lower data rates will require even less power ( $P_{req} \propto B^{1/2}$ ). Therefore, using the spherical-filter results of Table 2, the range of a 100-mW transmitter is less than 3 m at 100 Mb/s, but more than 4 m at 10 Mb/s, and more than 6 m at 1 Mb/s. In a wireless-LAN application, for example, the up link from portable computer to base station may have lower data-rate requirements than the down link, allowing the possibility of using low-power portable transmitters and higher-power fixed transmitters.

## V. SUMMARY and CONCLUSIONS

We performed a link-budget analysis for a short-range communication system using non-directed line-of-sight infrared radiation. We examined the performance of an optical front end comprising a thin-film spherical optical filter and a truncated spherical lens. A truncation angle of  $90^\circ$  was shown to minimize the angle-of-incidence spread for the

filter, thus approximately maximizing its field of view. An optimized hemispherical-filter front end was shown to outperform an optimized planar-filter front end by several optical dB when the lens radius is  $R = 2$  cm. This SNR improvement can be made arbitrarily large by choosing the lens radius suitably large, at the cost of increased size and weight. We presented a procedure for jointly optimizing the transmitter radiation pattern and receiver optical front end. Numerical results show that 269 mW of transmitted signal power is sufficient to achieve 100 Mb/s throughout a 4-m radius cell with high background irradiance.

Several problems remain unsolved. For example, the most practical means for implementing a transmitter with a prescribed radiation pattern is not known, although a likely candidate is to use a laser diode with a computer-generated hologram [7]. Because of its simplicity, this paper considered only the truncated spherical lens; a better design strategy would be to include the lens shape as a design parameter. In addition, we also made the line-of-sight assumption that the transmitter was a distant point source. Therefore, the relevance of our results to infrared links using extended sources, such as the ceiling in a typical diffuse link, should be examined. The impact on optical design of additional impediments, such as receiver tilt, shadowing, multipath dispersion, and electronic receiver noise, should also be explored. Finally, we remark that, when the size of a hemispherical thin-film filter is constrained to dimensions suitable for a portable receiver, the optimized bandwidth far exceeds the bandwidth of a modulated single-frequency laser. Therefore, in principle, further substantial improvements in performance could result from the development of a small, light-weight, wide-FOV, narrowband optical filter.

### Appendix A: Proof of Theorem 1

By contradiction. Let  $R_o(\psi)$  make the received power equal to the same constant at every point on the lines  $\overline{AB}$  and  $\overline{BC}$ , and suppose that  $R(\psi) = R_o(\psi) + \delta R(\psi)$  yields a higher minimum SNR, with  $\delta R(\psi)$  nonzero.

We first show that there exists an angle  $\psi^*$  such that  $\delta R(\psi^*) < 0$ . Both  $R_o(\psi)$  and  $R_o(\psi) + \delta(\psi)$  must satisfy the same power constraint of (22), so that:

$$1 = 2\pi \int_0^{\psi_C} R_o(\psi) \sin \psi \, d\psi + 2\pi \int_0^{\psi_C} \delta R(\psi) \sin \psi \, d\psi = 1 + 2\pi \int_0^{\psi_C} \delta R(\psi) \sin \psi \, d\psi. \quad (27)$$

The last integral must therefore be zero. Since  $\sin(\psi) > 0$  for all  $\psi \in (0, \psi_C)$ , there must exist an angle  $\psi^* \in (0, \psi_C)$  such that  $\delta R(\psi^*) < 0$ .

Next, define  $P_o$  as the constant received power on lines  $\overline{AB}$  and  $\overline{BC}$  when the transmitter radiation pattern is  $R_o(\psi)$ ; for any  $\psi \in (0, \psi_C)$ , it is specified by (23):

$$P_o = \frac{1}{h(\psi)^2} R_o(\psi) \cos^3 \psi A_{eff}(\psi). \quad (28)$$

Similarly, define  $P_1(\psi)$  as the received power at angle  $\psi$  on lines  $\overline{AB}$  and  $\overline{BC}$  when the radiation pattern is  $R_o(\psi) + \delta(\psi)$ :

$$P_1(\psi) = \frac{1}{h(\psi)^2} \{R_o(\psi) + \delta R(\psi)\} \cos^3 \psi A_{eff}(\psi) = P_o + \frac{1}{h(\psi)^2} \delta R(\psi) \cos^3 \psi A_{eff}(\psi). \quad (29)$$

In particular, at  $\psi = \psi^*$  we have:

$$P_1(\psi^*) = P_o + \frac{1}{h(\psi^*)^2} \delta R(\psi^*) \cos^3 \psi^* A_{eff}(\psi^*) < P_o, \quad (30)$$

where the last inequality follows because  $\delta R(\psi^*) < 0$  and  $\psi^* \in (0, \pi/2)$ . Thus, we see that any deviation from  $R_o(\psi)$  results in a reduced received signal power at some position  $\psi^*$ , which guarantees that  $R_o(\psi)$  maximizes the minimum SNR throughout the cell. ♦

## REFERENCES

- [1] F. R. Gfeller and U. H. Bapst, "Wireless In-House Data Communication via Diffuse Infrared Radiation," *Proceedings of the IEEE*, **67**:11, 1474-1486 (November 1979).
- [2] M. D. Kotzin, "Short-Range Communications Using Diffusely Scattered Infrared Radiation," Ph.D. Dissertation, Northwestern University (1981).
- [3] M. D. Kotzin and A. P. van den Heuvel, "A Duplex Infra-Red Systems for In-Building Communications," *IEEE VTC '86*, 179-185 (1986).
- [4] J. R. Barry, "Wireless Communication Using Non-Directed Infrared Radiation," Ph.D. Dissertation, University of California at Berkeley (December 1992).
- [5] D. R. Pauluzzi, P. R. McConnell, and R. L. Poulin, "Free-Space Undirected Infrared Voice and Data Communications with a Comparison to RF Systems," *Proc. IEEE International Conference on Selected Topics in Wireless Communications*, Vancouver, B. C., 279-285 (June 1992).
- [6] M. E. Marhic, M. D. Kotzin, and A. P. van den Heuvel, "Reflectors and Immersion Lenses for Detectors of Diffuse Radiation," *Journal of the Optical Society of America*, **72**:3, 352-355 (March 1982).
- [7] P. P. Smyth, M. McCullagh, D. Wisely, D. Wood, S. Ritchie, P. Eardley, and S. Cassidy, "Optical Wireless Local Area Networks — Enabling Technologies," *B. T. Technol. J.*, **11**:2 (April 1993).
- [8] J. M. Kahn, J. R. Barry, M. D. Audeh, J. B. Carruthers, W. J. Krause, and G. W. Marsh, "Non-Directed Infrared Links for High-Capacity Wireless LANs," *IEEE Personal Communications Magazine*, **1**:2, 12-25 (1994).
- [9] H. A. Ankermann, "Transmission of Audio Signals by Infrared Light Carrier," *SMPTE Journal*, **89**, 834-837 (November 1980).
- [10] S. Ramo, J. R. Whinnery, and T. Van Duzer, *Fields and Waves in Communication Electronics* (John Wiley & Sons, New York, 1984), Chap. 6, pp. 309-310.
- [11] H. A. Macleod, *Thin-Film Optical Filters* (Adam Hilger Ltd, London, 1969).

- [12] J. D. Rancourt, *Optical Thin Films* (Macmillan Publishing, New York, 1987).
- [13] Melles Griot Product Catalog (1991), Chap. 11, pp. 25-30.
- [14] OCLI Product Catalog (1990).
- [15] G. Smestad, H. Ries, R. Winston, and E. Yablonovitch, "The thermodynamic limits of light concentrators," *Solar Energy Materials*, **21**, 99-111 (1990).
- [16] G. W. Marsh and J. M. Kahn, "50-Mb/s Diffuse Infrared Free-Space Link using On-Off Keying with Decision Feedback Equalization," to appear, *IEEE Photon. Technol. Lett.* **6**:10 (October 1994).
- [17] J. P. Savicki and S. P. Morgan, "Hemispherical Concentrators and Spectral Filters for Planar Sensors in Diffuse Radiation Fields," submitted to *Applied Optics* (1993).
- [18] E. D. Palik, ed., *Handbook of Optical Constants of Solids* (Orlando, Academic Press, 1985), p. 565.
- [19] IEC825: "Radiation Safety of Laser Products' Equipment Classification, Requirements, and User's Guide" (1984), plus amendments 1 (1990) and 2 (1994).

#### LIST OF TABLE CAPTIONS

Table 1: Transmission Calculations for Fig. 6.

Table 2: Sample Optimization Results.

## LIST OF FIGURE CAPTIONS

- Fig. 1. Comparison between actual transmission and analytical model of (8) with  $\Delta\lambda = 36.3$  nm,  $\lambda_{normal} = 850$  nm,  $n_s = 2.293$ ,  $m = 3$ , and  $T_0 = 0.92$ .
- Fig. 2. Dependence of center wavelength on angle of incidence for the filter of Fig. 1. Barely discernible is the analytic approximation of (6) with  $n_s / n_1 = 2.293$ .
- Fig. 3. Filter transmission at  $\lambda_0 = 810$  nm as a function of angle of incidence for filter of Fig. 1: actual (solid curve) and analytical model (dashed curve, from (8) with  $\Delta\lambda = 36.3$  nm,  $m = 3$ ,  $T_0 = 0.92$ ,  $\lambda_{normal} = 850$  nm and  $n_s / n_1 = 2.293$ , or  $\hat{\theta} = 44^\circ$ ).
- Fig. 4. Proposed receiver optics for (a) planar filter and (b) spherical filter; (c) shows an expanded schematic diagram for both cases.
- Fig. 5. Dependence of normal-incidence gain and on lens radius, assuming  $\theta_t = 90^\circ$ , no reflections,  $A = 1$  cm<sup>2</sup>, and  $\psi = 0^\circ$ . Also shown is maximum angle of incidence, as defined in Sect. III-C, assuming  $\theta_t = 90^\circ$ ,  $A = 1$  cm<sup>2</sup> and  $\psi \in [0, \pi/2)$ .
- Fig. 6. Dependence of gain on angle of incidence: (a)  $\theta_t = 70^\circ$ ; (b)  $\theta_t = 90^\circ$ ; (c)  $\theta_t = 110^\circ$ .
- Fig. 7. Density functions (a) at lens input; (b) at lens output. ( $\theta_t = 90^\circ$ ,  $R = 2$  cm,  $n = 1.8$ ,  $A = 1$  cm<sup>2</sup>.)
- Fig. 8. Cross-sectional view of coverage area.
- Fig. 9. Optimal transmitter radiation patterns and effective areas for 4-m cell radius: (a) and (b) planar filter; (c) and (d) hemispherical filter.
- Fig. 10. Required transmitter optical power versus cell radius.

## TABLES

TABLE 1: Transmission Calculations for Fig. 6.

	Ideal	Uncoated	Coated	Planar	Spherical
$T(\theta_0)$	1	From (1)—(5) with $n_1 = 1, n_2 = 1.8$	From (1)—(5) with $n_1 = 1, n_2 = 1.38,$ $d_2 = 1.04, n_3 = 1.8$	From (1)—(5) with $n_1 = 1, n_2 = 1.38,$ $d_2 = 1.04, n_3 = 1.8$	From (8) with $\Delta\lambda = 15 \text{ nm},$ $\hat{\theta} = 15^\circ, T_0 = 0.7,$ $m = 3, n_s/n_1 = 2.293$
$T(\theta_2)$	1	From (1)—(5) with $n_1 = 1.8, n_2 = 1$	1	1	1
$T(\theta_3)$	1	1	1	From (8) with $\Delta\lambda = 15 \text{ nm}, \hat{\theta} = 45^\circ,$ $T_0 = 0.7, m = 3,$ $n_s/n_1 = 2.293$	1
$T(\theta_4)$	1	From (1)—(5) with $n_1 = 1, n_2 = 3.686$	From (1)—(5) with $n_1 = 1.8, n_2 = 2.0,$ $d_2 = 1.42, n_3 = 3.686$	From (1)—(5) with $n_1 = 1.8, n_2 = 2.0,$ $d_2 = 1.42, n_3 = 3.686$	From (1)—(5) with $n_1 = 1.8, n_2 = 2.0,$ $d_2 = 1.42, n_3 = 3.686$

TABLE 2: Sample Optimization Results.

parameter	planar filter				hemispherical filter				units
	3-m radius	4-m radius	5-m radius	8-m radius	3-m radius	4-m radius	5-m radius	8-m radius	
$\Delta\lambda$	66.0	70.1	70.6	66.4	14.1	12.3	10.7	7.5	nm
$\hat{\theta}$	44.5°	49.4°	52.7°	58.7°	17.0°	15.6°	14.4°	11.8°	degrees
$d_{c,1}$	1.002	1.125	1.064	1.035	—	—	—	—	QWOT
$d_{c,2}$	1.511	1.510	1.515	1.535	1.414	1.605	1.758	2.014	QWOT
$P_o/P$	2.03	0.94	0.50	0.124	2.00	0.90	0.47	0.107	$\times 10^{-6}$
$P_{req}$	276	614	1,159	4,532	130	269	564	1,765	mW

Assumptions:  $\theta_t = 90^\circ$ ,  $n = 1.8$ ,  $R = 2$  cm,  $A = 1$  cm<sup>2</sup>,  $\lambda_0 = 810$  nm, Butterworth  $m = 3$ ,  $n_s/n_1 = 2.293$ ,

$T_0 = 0.7$ ,  $n_{m,3} = n_{m,4} = 1.8$ ,  $n_{c,1} = 1.38$ ,  $n_{c,2} = 2.0$ ,  $n_d = 3.686$ ,  $h_{min} = 1.5$  m,  $h_{max} = 2.4$  m,

$p_{bg} = 5.8$   $\mu$ W/(cm<sup>2</sup>nm),  $r = 0.53$  A/W,  $B = 100$  MHz, SNR = 13.5 dB.

## FIGURES

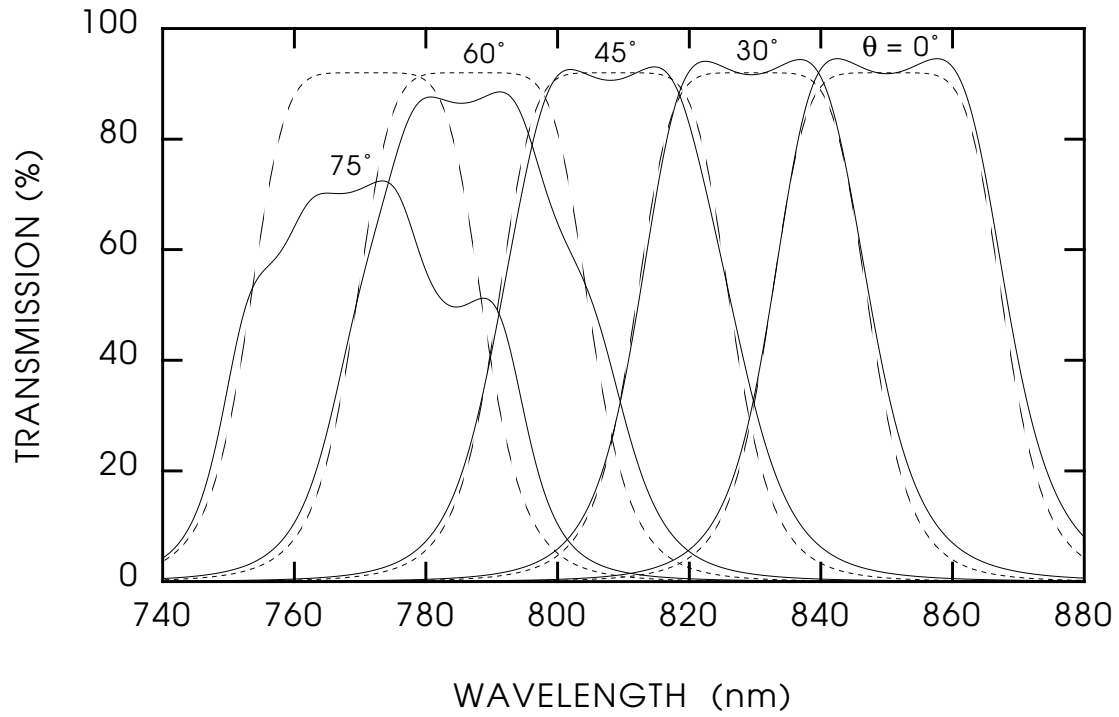


Fig. 1. Comparison between actual transmission and analytical model of (8) with  $\Delta\lambda = 36.3$  nm,  $\lambda_{normal} = 850$  nm,  $n_s = 2.293$ ,  $m = 3$ , and  $T_0 = 0.92$ .

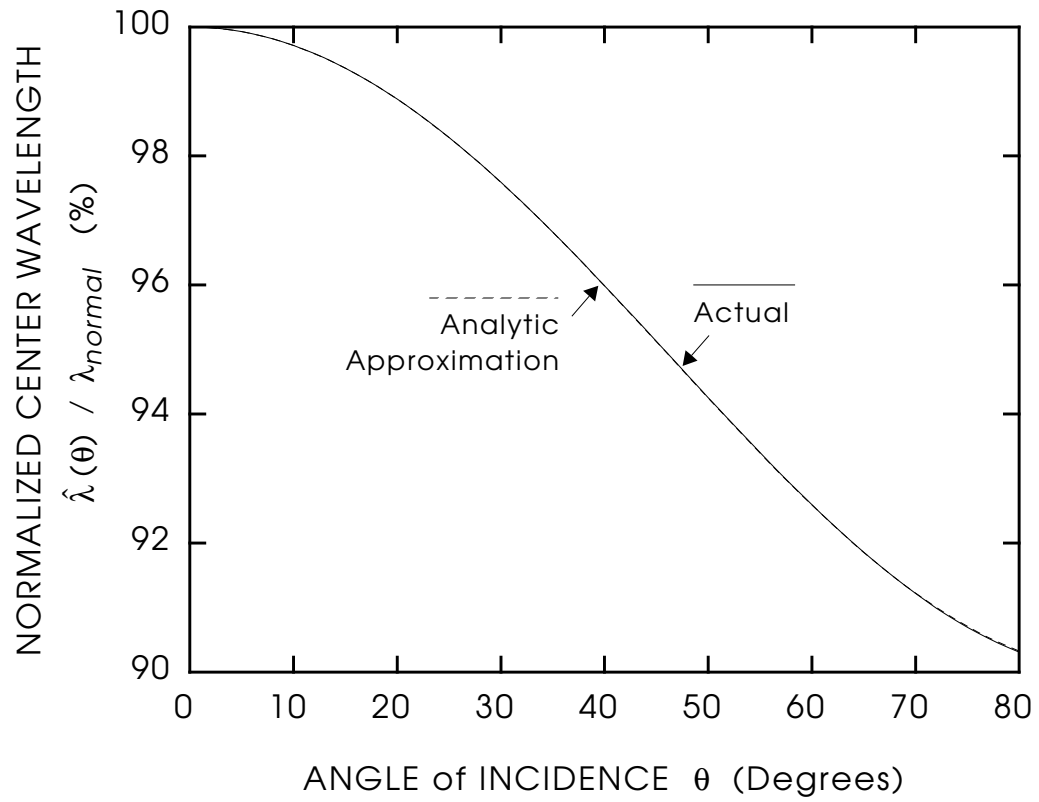


Fig. 2. Dependence of center wavelength on angle of incidence for the filter of Fig. 1. Barely discernible is the analytic approximation of (6) with  $n_s/n_1 = 2.293$ .

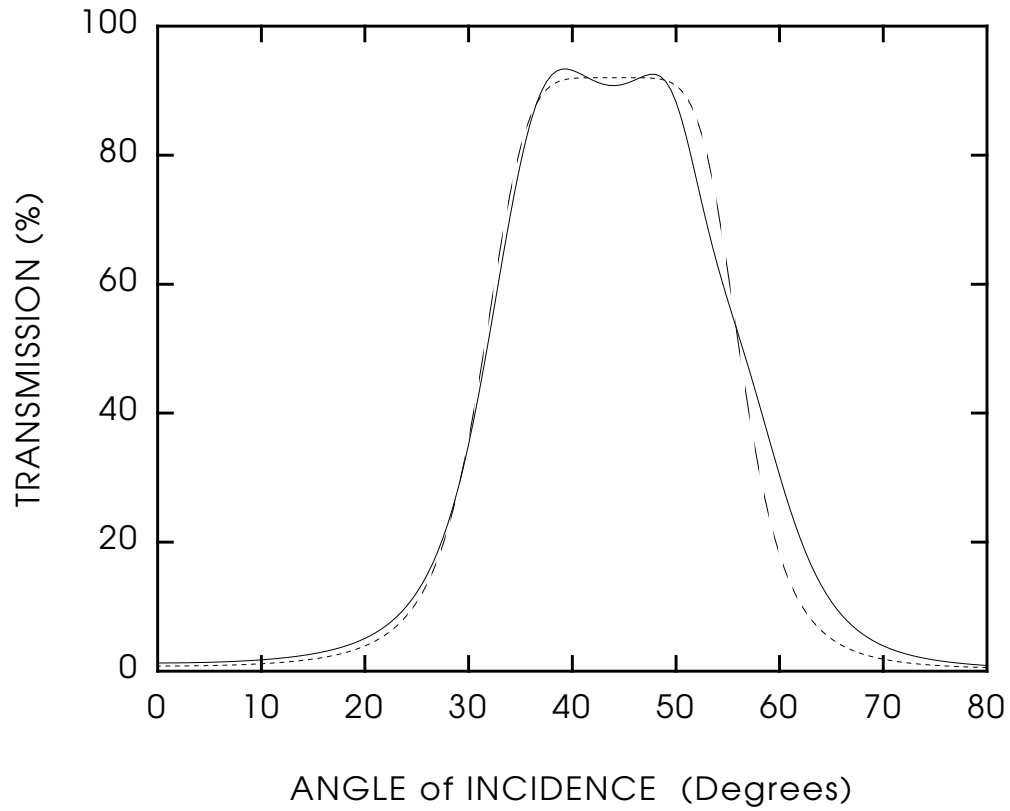
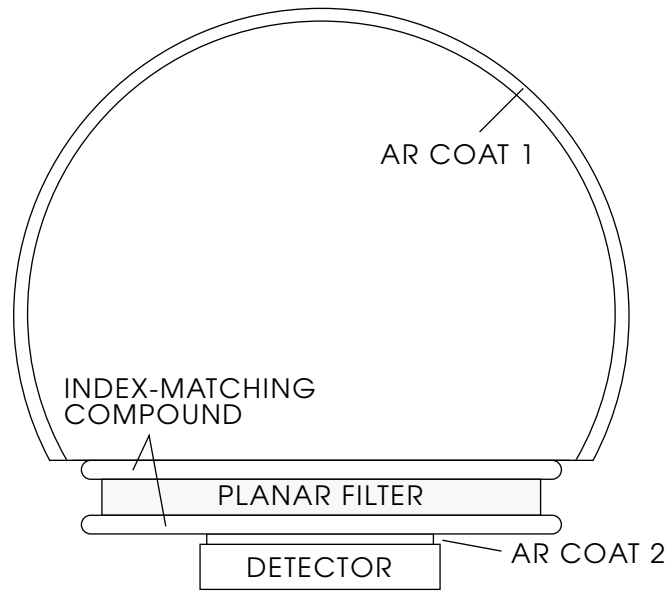
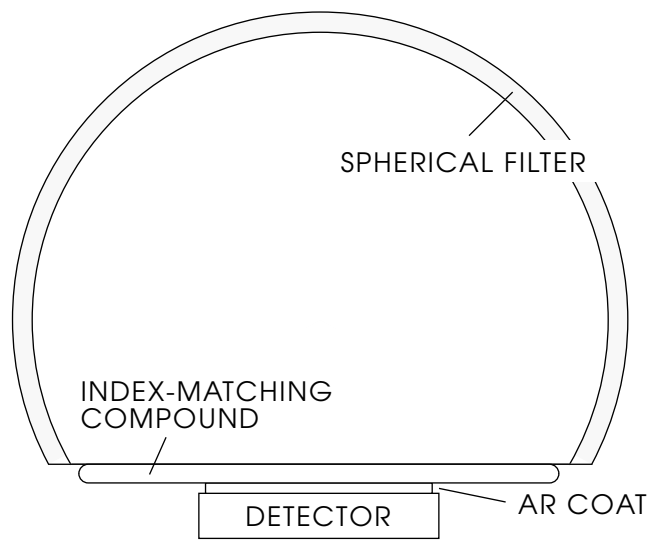


Fig. 3. Filter transmission at  $\lambda_0 = 810$  nm as a function of angle of incidence for filter of Fig. 1: actual (solid curve) and analytical model (dashed curve, from (8) with  $\Delta\lambda = 36.3$  nm,  $m = 3$ ,  $T_0 = 0.92$ ,  $\lambda_{normal} = 850$  nm and  $n_s/n_1 = 2.293$ , or  $\hat{\theta} = 44^\circ$ ).

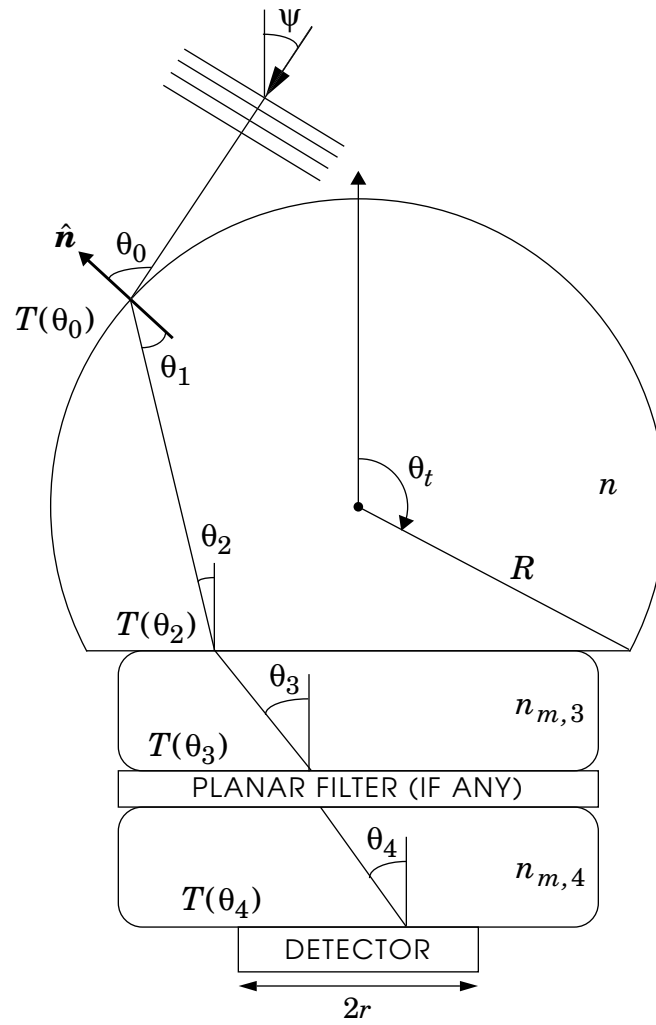


(a)



(b)

Fig. 4. Proposed receiver optics for (a) planar filter and (b) spherical filter; (c) shows an expanded schematic diagram for both cases.



(c)

Fig. 4, continued: (c).

Proposed receiver optics for (a) planar filter and (b) spherical filter; (c) shows an expanded schematic diagram for both cases.

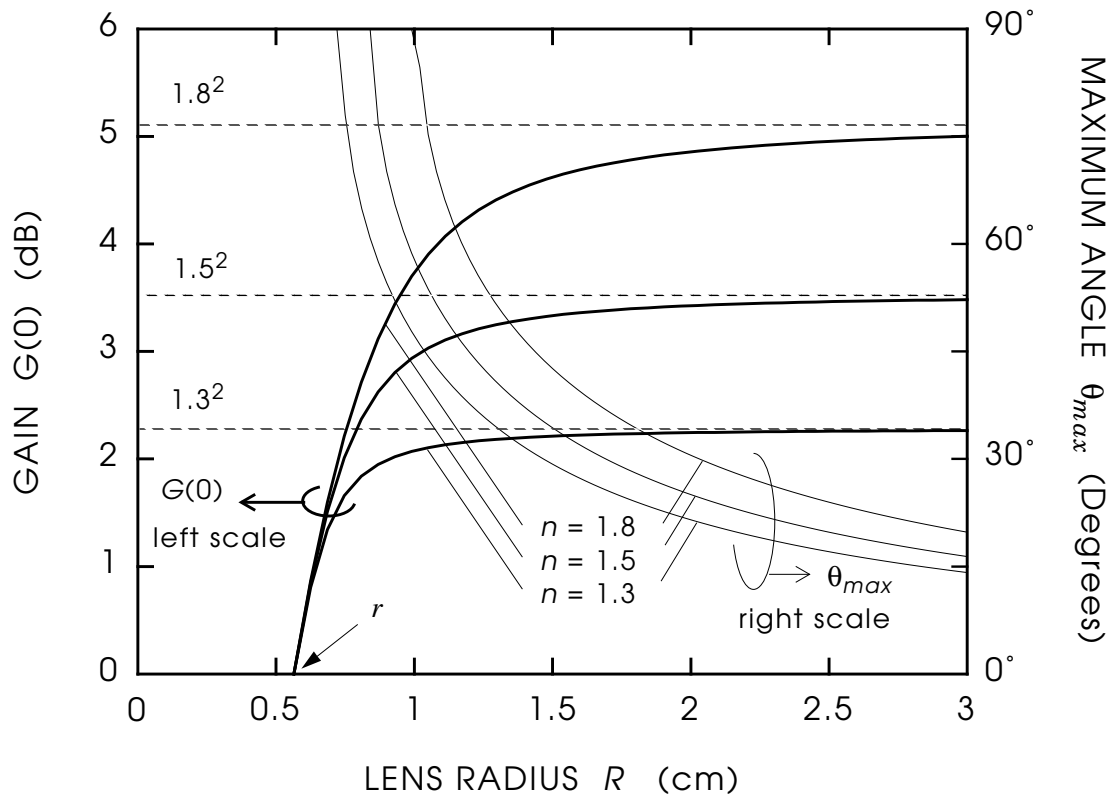


Fig. 5. Dependence of normal-incidence gain and on lens radius, assuming  $\theta_t = 90^\circ$ , no reflections,  $A = 1 \text{ cm}^2$ , and  $\psi = 0^\circ$ . Also shown is maximum angle of incidence, as defined in Sect.III-C, assuming  $\theta_t = 90^\circ$ ,  $A = 1 \text{ cm}^2$  and  $\psi \in [0, \pi/2)$ .

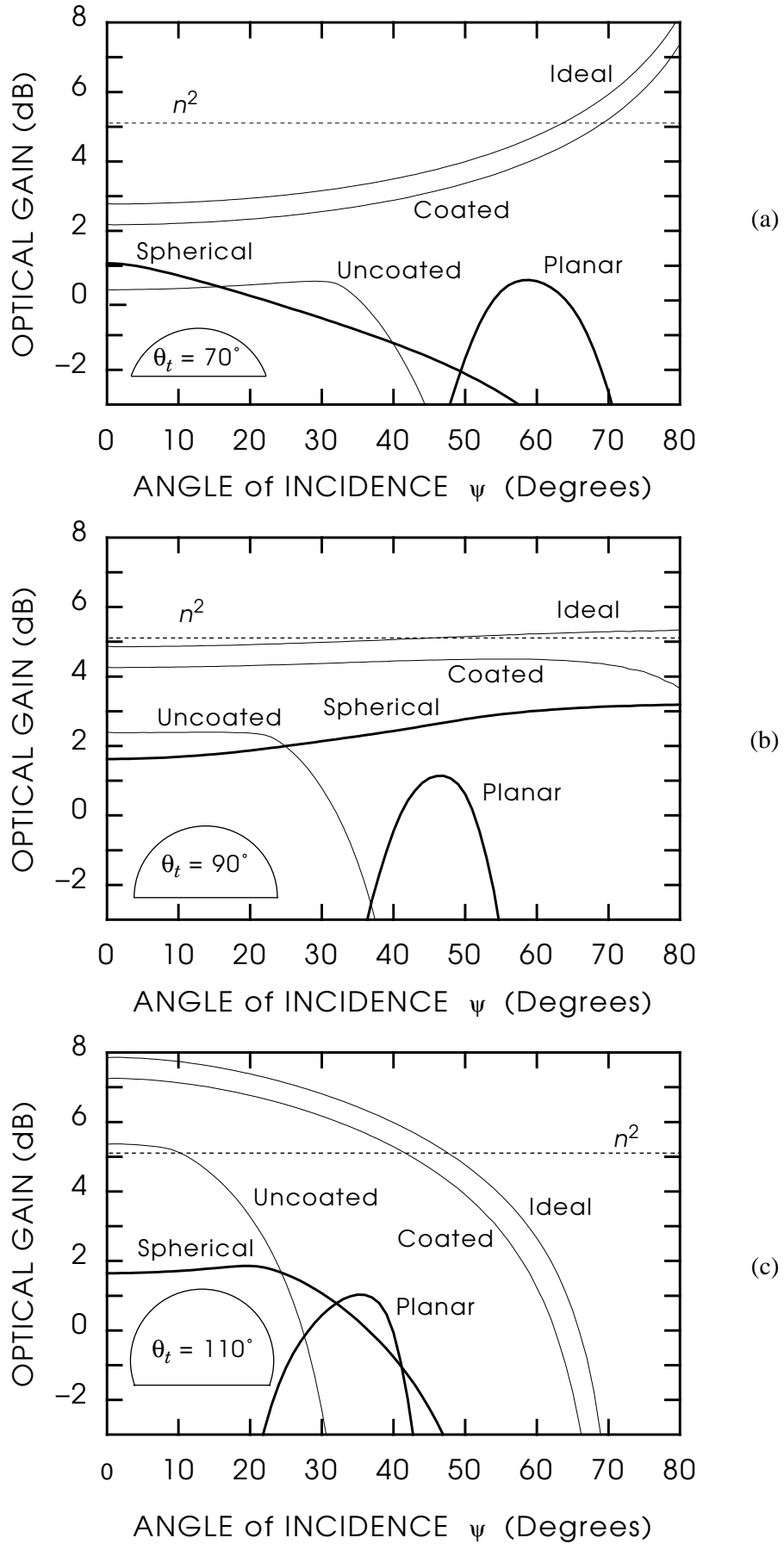
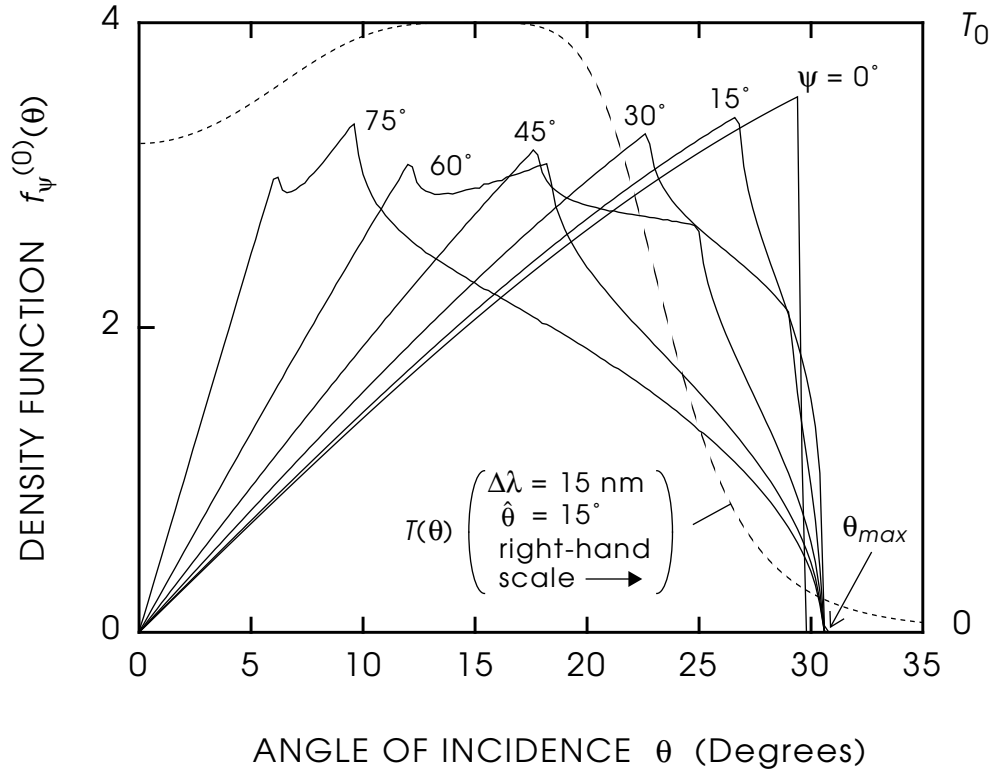
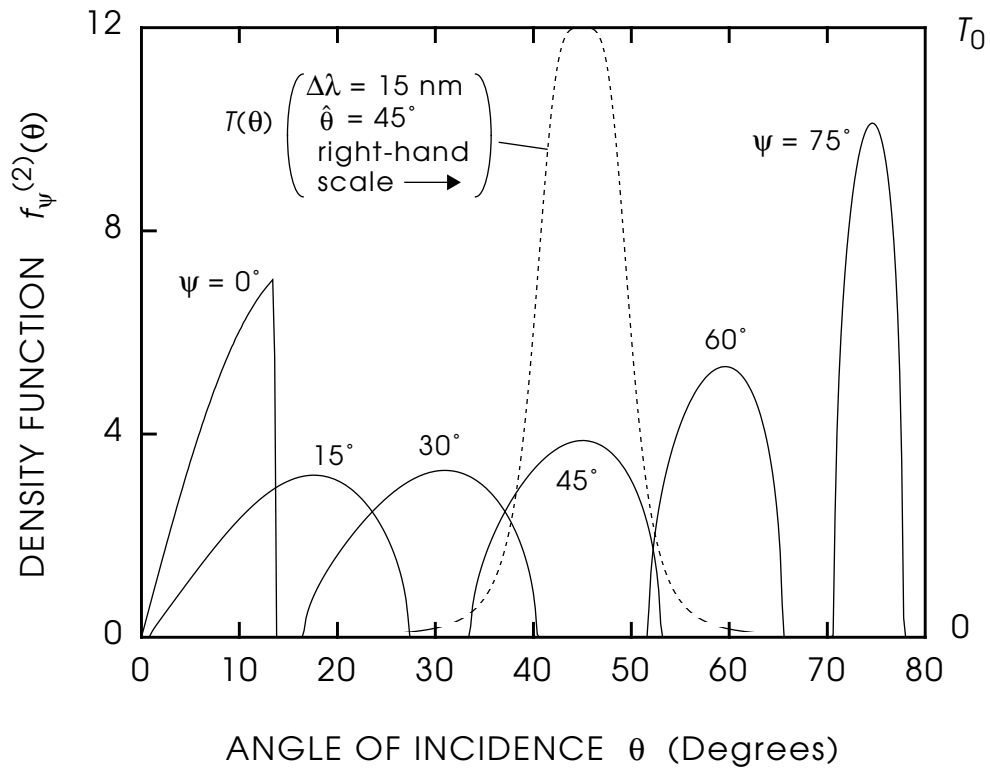


Fig. 6. Dependence of gain on angle of incidence: (a)  $\theta_t = 70^\circ$ ; (b)  $\theta_t = 90^\circ$ ; (c)  $\theta_t = 110^\circ$ .



(a)



(b)

Fig. 7. Density functions (a) at lens input; (b) at lens output. ( $\theta_t = 90^\circ$ ,  $R = 2 \text{ cm}$ ,  $n = 1.8$ ,  $A = 1 \text{ cm}^2$ .)

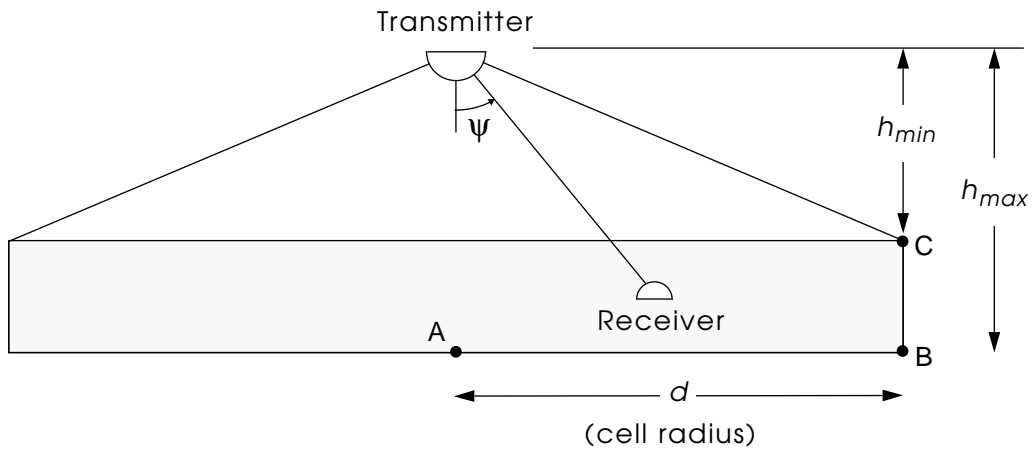


Fig. 8. Cross-sectional view of coverage area.

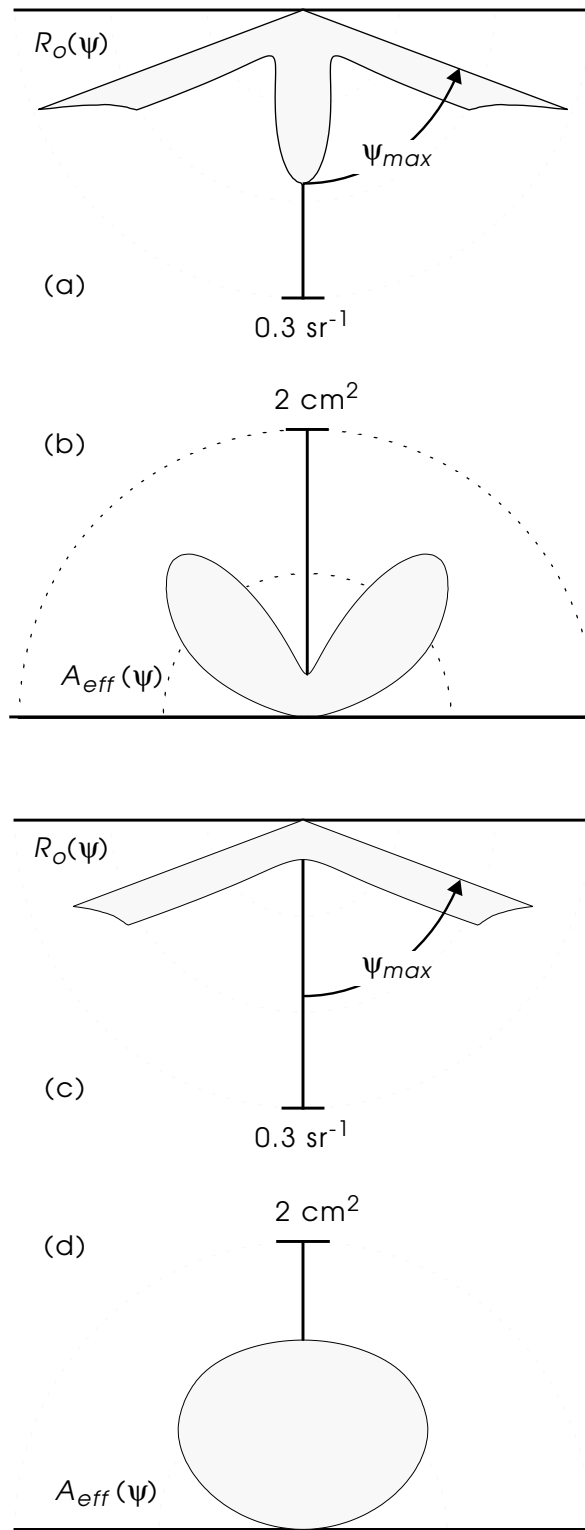


Fig. 9. Optimal transmitter radiation patterns and effective areas for 4-m cell radius:

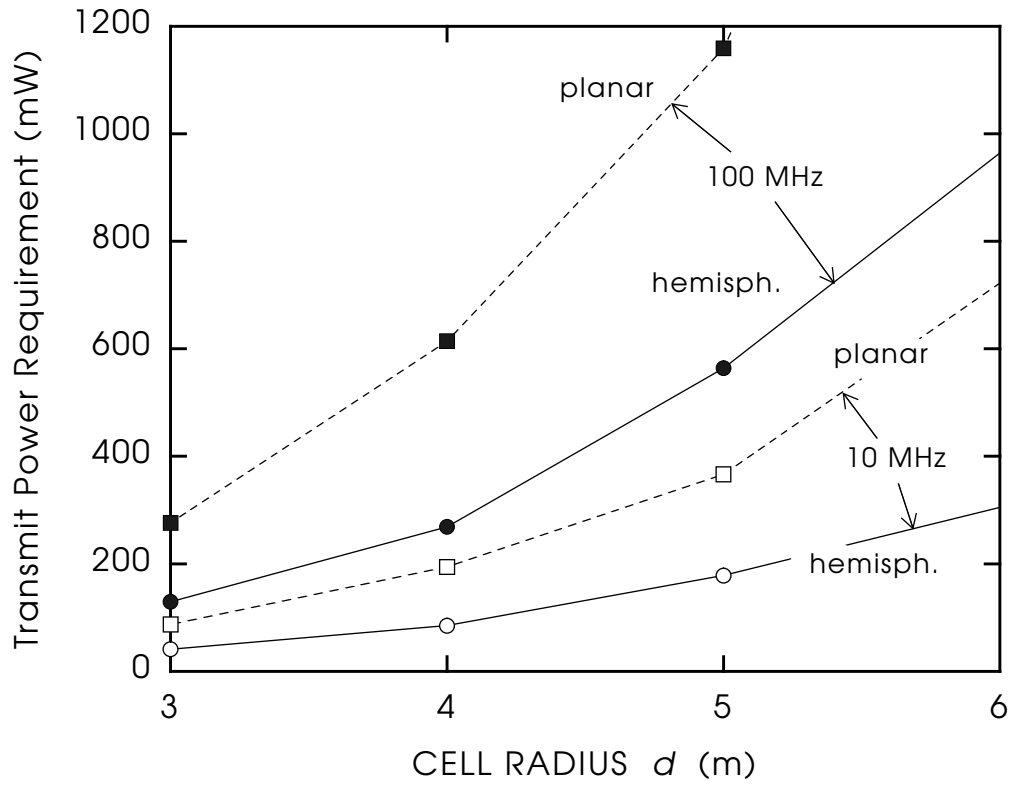


Fig. 10. Required transmitter optical power versus cell radius.